Journal of Solid State Electrochemistry
https://doi.org/10.1007/s10008-026-06668-z

ORIGINAL PAPER

Investigation of PEO as an alternative non-fluorinated binder for P2-NFMO cathode material for SIBs

Anna Domgans[1,2] · Nabi Aghdassi[1] · Tobias Braun[1,2] · Luc Raijmakers[1] · Anna Windmüller[1] · Rüdiger-A. Eichel[1,2]

Received: 16 June 2026 / Revised: 17 July 2026 / Accepted: 19 July 2026
© The Author(s), under exclusive licence to Springer-Verlag GmbH Germany, part of Springer Nature 2026

Abstract
Poly(vinylidene fluoride) is a widely used binder for cathodes in lithium-ion and sodium-ion batteries. However, poly(vinylidene fluoride) is sensitive to base-induced decomposition via defluorination, which can negatively impact electrochemical performance. This issue is particularly pronounced in sodium-ion batteries due to the higher basicity of sodium, underscoring the need for alternative binder systems. In this work, poly(vinylidene fluoride) and poly(ethylene oxide) are investigated as binders for a P2-$Na_{2/3}Mn_{2/3}Fe_{1/3}O_2$ cathode material, with poly(ethylene oxide) selected as a fluorine-free alternative to poly(vinylidene fluoride) due to its favorable ionic conductivity, mechanical properties, affordability, and environmental compatibility, thereby enabling a systematic comparison between fluorinated and fluorine-free binders. Fourier-Transform Infrared Spectroscopy revealed structural changes in poly(vinylidene fluoride) during slurry preparation, whereas poly(ethylene oxide) remained unaffected. X-ray Photoelectron Spectroscopy analysis confirmed the chemical and electrochemical stability of poly(ethylene oxide), while NaF formation provided clear evidence for poly(vinylidene fluoride) defluorination and its further degradation during cycling. Galvanostatic charge/discharge measurements showed an improvement in capacity retention of 5.8% after 100 cycles for poly(ethylene oxide) -based electrodes compared to poly(vinylidene fluoride), demonstrating the detrimental impact of poly(vinylidene fluoride) degradation on electrochemical performance. These findings highlight the importance of developing chemically stable binder systems for sodium-ion batteries.

Keywords Sodium-ion-batteries · Non-aqueous binders · Deflourination of poly(vinylidene fluoride) · X-ray powder diffraction · Fourier-Transform Infrared Spectroscopy · X-ray Photoelectron Spectroscopy

Introduction

Global energy demand is constantly increasing, while the effects of the climate crisis are becoming ever more apparent. To effectively utilize renewable energy sources such as solar, wind and tidal, efficient and sustainable storage technologies are essential [1]. Lithium-ion batteries (LIBs) currently dominate the market, but Li is a limited and expensive metal [2]. Na, on the other hand, is widely available as an alkali metal, is inexpensive and ecologically more advantageous. Sodium-ion batteries (SIBs) are therefore considered a promising side-by-side technology to LIBs, especially for large-scale stationary energy storage or in electric vehicles [2].

The development of SIBs involves different challenges to those of LIBs, as Na and Li differ in several important properties. These include their ionic radius (Na = 0.98 Å, Li = 0.69 Å), their redox potential (Na = -2.71 V vs. SHE, Li = -3.05 V vs. SHE) and their atomic weight (Na = 22.98 g/mol, Li = 6.94 g/mol) [3]. The larger ionic radius of Na leads to greater volume expansion during charge and discharge cycles, which can affect the mechanical stability and overall lifetime of the battery. In addition, the lower mobility of Na ions leads to more sluggish kinetic reactions, which can limit the charge and discharge rate [3]. The larger atomic mass of Na also affects the energy density of SIBs, as the

✉ Anna Domgans
a.domgans@fz-juelich.de

[1] Institute for Energy Technologies (IET-1 Fundamental Electrochemistry), Forschungszentrum Jülich, Jülich 52425, Germany

[2] Material and Processes of Electrochemical Energy Storage and Conversion, RWTH Aachen University, Aachen, Germany

Published online: 25 July 2026

heavier Na ions reduce the total amount of energy stored per unit volume or weight, giving SIBs a lower energy density compared to LIBs. Achieving efficiency, charging times and overall energy performance comparable to conventional LIBs thus remains demanding. On the other hand, SIBs offer significant advantages. One key benefit is that Na is an abundant metal in the Earth's crust, as it is found in a variety of minerals [4, 5]. Additionally, Al can be used as a current collector since, unlike Li, Na does not form alloys with Al [6]. There is also the potential to use resource-efficient and non-toxic metals such as Fe and Mn [5]. Consequently, the development of suitable materials for SIBs, especially for the cathode, is essential to exploit the potential of SIBs and improve their performance, efficiency and sustainability.

Layered transition metal oxides (LTMOs) have proven to be promising cathode materials due to their high specific capacity, the use of resource-efficient materials and ease of synthesis [3]. The general formula for LTMOs is Na_xMO_2 (where M = Mn, Fe, Ni or Co). These compounds usually consist of alternating layers of Na ions and MO_6 octahedra. Within the family of LTMOs, two main types can be distinguished: P2 and O3 [7]. These differ in Na content, stacking order of the oxide layers and the synthesis temperature. In the structure of type P2, Na ions occupy prismatic sites between the MO_2 layers. This type crystallizes in the hexagonal space group $P6_3/mmc$ and remains structurally stable if the Na content is in the range of $0.67 < x < 0.85$ per formula unit [3, 8, 9]. In contrast, the structure of type O3 has Na ions in octahedral coordination. It crystallizes in the rhombohedral space group $R\bar{3}m$ and normally contains $x = 1$ Na ion per formula unit [9]. Both P2- and O3- LTMOs undergo phase transitions during charge and discharge cycles leading to significant loss of capacity and structural instability [3, 8, 9]. These transitions are primarily due to the sliding of the TM layers during sodiation/desodation, resulting in irreversible structural changes that lead to a strong loss of capacity. In addition, LTMOs are sensitive to air and moisture [10, 11]. Exposure to moisture and CO_2 from the atmosphere can lead to the formation of surface layers of NaOH and Na_2CO_3. Besides, H_2O can promote a proton exchange process in which Na ions are replaced by H-ions in the interlayer spacing. This exchange changes the interlayer spacing and can lead to layer displacements that further compromise the structural integrity and electrochemical performance of the material [8, 10]. In this study, we used the Fe/Mn-based P2-$Na_{2/3}Fe_{1/3}Mn_{2/3}O_2$ (NFMO) cathode material to investigate different binders, as it can deliver a capacity of up to 193 mAh g^{-1} and exhibits a capacity retention of 79% after 40 cycles between 1.5 and 4.3 V vs. Na/Na^+ [12].

In addition to the development of suitable cathode materials, the choice of the binder also plays a decisive role in the performance of SIBs, although it only accounts for a small portion of the electrode in terms of quantity [13]. Binders ensure the mechanical integrity of the electrode, influence its electrochemical properties and contribute to long-term stability [14, 15]. Careful selection of the binder is particularly important for SIBs, where cathode materials are sensitive to air and moisture. The main function of binders is to provide mechanical integrity of the electrode by strong adhesion between its components. This prevents the active material from detaching from the electrode structure or suspending in the electrolyte during charge and discharge cycles. Properties of binders such as strength, elasticity, flexibility, and hardness are thus very important [16].

Binders can be divided into aqueous and non-aqueous types based on the solvent used in electrode preparation. Common aqueous binders include styrene-butadiene rubber (SBR), poly(acrylic acid) (PAA), sodium alginate (SA), and carboxymethyl cellulose (CMC). PAA, SA and CMC are often used for anodes, although their mechanical properties are lacking. However, favorably, their carboxyl groups make them water-soluble and ensure strong adhesion [17]. Since LTMOs are sensitive to air and moisture, the use of water-based binders poses a challenge. Their tendency to hydrate leads to water absorption, which causes a proton exchange from Na to H. This process alters the distance between the structural layers and causes layer displacement, both of which can promote unfavorable phase transitions and impair structural stability [15].

In contrast, non-aqueous binders include polytetrafluoroethylene (PTFE), polyimide (PI), polyacrylonitrile (PAN), poly(vinylidene fluoride) (PVDF), and poly(ethylene oxide) (PEO). PTFE exhibits good chemical and thermal stability and is ideal for use in solvent-free electrodes. However, PTFE can react with the electrolyte, resulting in a significant loss of capacity and low initial charge efficiency [16]. PVDF is a widely used non-aqueous binder in LIBs and SIBs due to its excellent chemical, thermal, and electrochemical stability, as well as its good mechanical properties and processability [16, 18–20]. However, its low ionic conductivity and poor adhesion can negatively affect the electrochemical performance of the electrode [16, 18–20]. It also requires the use of the toxic and expensive solvent N-methyl-2-pyrrolidone (NMP) for electrode processing, which is volatile, environmentally harmful, and difficult to degrade [13, 14]. PVDF is stable under acidic conditions, but reacts strongly under alkaline conditions, which is particularly problematic in SIBs, as NaOH is more alkaline than LiOH [21]. A reaction with strong bases leads to defluorination of PVDF, in which HF is released and cross-linked structures form, impairing the binding function of the material [13, 14]. If Na-containing LTMOs are used, which form surface NaOH upon exposure to moisture, NaOH reacts with PVDF during

slurry preparation, leading to an inhomogeneous mixture and gel formation [16]. In addition, the formation of NaF as a reaction product weakens the integrity of the electrode [16, 22].

PEO is mainly used as a solid electrolyte in all-solid-state batteries because it exhibits outstanding ionic conductivity but poor resistance to oxidation at high potentials. In LIBs and SIBs, PEO is also used as a binder for anodes, while its use in cathodes is less common [17]. In a study on PEO used as a binder for SIBs, significant improvements in Na ion conductivity and performance were observed [23]. These enhancements were primarily due to the high Na-ion diffusion coefficient of PEO. Moreover, the suppression of electrode swelling contributed to improved cycling stability and rate capability, further boosting the electrochemical performance of the battery [23]. In another study, PEO was used as a binder for $LiNi_{0.6}Co_{0.2}Mn_{0.2}O_2$ cathodes, showing that adhesion, electrode integrity, and electrochemical performance were improved using this polymer. The addition of 20 wt% PEO increased the capacity at 2 C from 131.1 mAh g^{-1} to 147.3 mAh g^{-1}, improved cycle stability, and reduced electrode resistance [20].

In this study, the cathode material P2-$Na_{2/3}Mn_{2/3}Fe_{1/3}O_2$ was employed to investigate the influence of fluorinated and non-fluorinated binder systems by using PVDF and PEO, respectively. Owing to its high ionic conductivity, mechanical flexibility, low cost, and environmental compatibility, PEO was selected as a representative non-fluorinated binder to enable a systematic comparison with PVDF [20]. The objective of this study is to compare the impact of base-induced defluorination on electrochemical performance via comparing PVDF with the fluorine free PEO system. To this end, a variety of analytical techniques are employed, including X-ray Diffraction (XRD) and Fourier-Transform Infrared Spectroscopy (FT-IR) of pure polymers, and polymer slurry solutions. Furthermore, X-ray Photoelectron Spectroscopy (XPS) measurements are conducted at varying charge states to investigate the electrochemical composition of these polymers. Finally, the influence on the electrochemical behavior of these binders is investigated through cyclic voltammetry measurements, C-rate tests, and long-term measurements.

Experimental

Synthesis

P2-$Na_{2/3}Mn_{2/3}Fe_{1/3}O_2$ (NFMO) was synthesized by a two-step solid-state reaction, as previously reported [24]. The precursors Na_2CO_3 decahydrate, Fe_2O_3 and MnO_2 were mixed in a motar grinder (Retsch RM 200). The mixed powder was transferred into a crucible and calcined in air at 600 °C for 8 h. The calcined powder was mixed again and then pressed into a pellet and sintered in air at 900 °C for 12 h. The pellet was cooled to room temperature, ground in a mortar, and immediately transferred into an argon-filled glove box to protect the powder from moisture.

Table 1 Sample name and compositions of the XRD samples

Sample	Composition
NFMO	$Na_{0.66}Fe_{1/3}Mn_{2/3}O_2$
NFMO + Electrolyte	$Na_{0.66}Fe_{1/3}Mn_{2/3}O_2$ + $NaBF_4$/$NaPF_6$/ diglyme
PVDF-Slurry	$Na_{0.66}Fe_{1/3}Mn_{2/3}O_2$ + PVDF/Carbon Black
PVDF-Slurry + Electrolyte	$Na_{0.66}Fe_{1/3}Mn_{2/3}O_2$ + PVDF/Carbon Black + $NaBF_4$/$NaPF_6$/diglyme
PEO-Slurry	$Na_{0.66}Fe_{1/3}Mn_{2/3}O_2$ + PEO/$NaPF_6$/ Carbon Black
PEO-Slurry + Electrolyte	$Na_{0.66}Fe_{1/3}Mn_{2/3}O_2$ + PEO/$NaPF_6$/ Carbon Black + $NaBF_4$/$NaPF_6$/diglyme

X-ray powder diffraction

The samples listed in Table 1 were measured to investigate the different behaviors of the binders PVDF and PEO. The PXRD patterns were recorded with a lab diffractometer (Empyrean, Panalytical) with a molybdenum anode (K_α wavelength 0.7107 Å). The samples were prepared between Kaptonfoils and the measurements were carried out in a Debye-Scherrer geometry. All samples were measured in a range of 5–55 2θ with a step size of 0.0084 counts. An internal standard of Al_2O_3 was mixed with all samples. Consequently, the size/strain and lattice parameters of the pristine Al_2O_3 were initially determined using the Pawley method. With these determined and fixed values, the lattice parameters for NFMO in all samples were subsequently determined again using the Pawley method and phase traction using QPA. The Pawley method and QPA based on the PXRD data was performed using the Diffrac.Topas Version 7 software package (Bruker).

Fourier-Transform Infrared Spectroscopy

For the FT-IR measurements, NFMO, PVDF powder, PEO powder, slurry of P2-$Na_{0.66}Mn_{2/3}Fe_{1/3}O_2$ with PVDF and PEO were mixed with KBr powder and subsequently pressed into pellets, each with a diameter of 11 mm. FT-IR spectra were recorded with a Bruker spectrometer (model Vertex 80v) in transmission mode on all pellets with the beam path fully evacuated ($p \leq 2.4$ mbar). A background recorded beforehand on an empty pellet holder was subtracted from the raw data obtained for each sample.

X-ray Photoelectron Spectroscopy

XPS was carried out by nanoAnalytics GmbH, Germany, on the pristine cathode sample, at Open Circuit Voltage (OCV), 1.5 V, and 4.2 V with PVDF binder, as well as on the pristine cathode sample, at OCV and 4.0 V with PEO binder. An ultra-high vacuum (UHV) set-up with a base pressure of E-9 mbar equipped with a monochromatic Al Kα X-ray source (hν = 1486.6 eV) and a high-resolution hemispherical electron analyzer (system NEXSA G2, Thermo Fisher Scientific Inc.) was used. Simultaneous supply of electrons and argon ions by an electron flood gun (0.2 eV at 100 µA) and an argon ion source, respectively, was employed for charge compensation for all samples. The X-ray spot diameter was 400 µm. Survey spectra and high-resolution scans were acquired with pass energies of 200 eV and 30 eV, respectively.

XPS data were processed using the CasaXPS software. Peak fitting of all high-resolution spectra was performed by minimizing the residual root mean square upon subtraction of a Shirley background. Percentage errors were estimated using Monte Carlo simulations.

C1s:

Spectra were fitted with up to six symmetric peaks and one asymmetric peak attributed to carbon in sp^2 C–C configuration (if applicable). Binding-energy (BE) constraints were applied as follows: the relative BE positions of C–O, C–O–C, CH_2–CF_2 and R–C = O, O–C–O, C–F peaks, each w.r.t. to the C-C/C-H peak, were constrained to 1.5 ± 0.1 eV and 2.9 ± 0.1 eV, respectively [25–28]. Equal Full Widths at Half Maximum (FWHMs) within an error margin of ± 0.1 eV were assumed for all symmetric peaks. The corresponding Voigt-like LA(1,1,735) line shape was obtained by fitting the C 1s region of a PEO powder reference sample with four peaks and equal FWHMs (Figure 5 Supporting Information). The sp^2 C–C contribution, in turn, was fitted using a synthetic asymmetric LF(0.69075, 1.17295, 113.304, 108) line shape obtained by fitting a carbon-black reference sample (without shake-up features).

F1s:

Up to three peaks with equal FWHMs (within an error margin of ± 0.1 eV) and without BE constraints were employed. The Voigt-like LA(1,1,520) line shape was obtained by fitting the F 1s region of a PVDF reference sample with a single peak.

O1s:

O1s regions were fitted with up to three peaks denoting different oxygen species and an additional Na KLL Auger peak (excluded from quantification) ppeak without any BE constraints. The FWHM of the NFMO lattice oxide peak was constrained to 1.1 ± 0.1 eV (based on the FWHM (≈ 1.1 eV) obtained for a NFMO reference sample), whereas equal FWHMs were assumed for the remaining oxygen species. Voigt-like LA(1,1,1401) line shapes were used for all peaks.

P2p:

Data were fitted with two doublets, each with a spin-orbit splitting ΔE = 0.86 and without BE constraints. Equal FWHMs and Voigt-like LA(1,1,611) line shapes (as obtained by fitting the P 2p region of a $NaPF_6$ reference sample with a single doublet) were employed for all P $2p_{3/2}$ and P $2p_{1/2}$ peaks.

Electrochemical measurement

Slurry preparation

For the preparation of electrodes with PVDF as a binder, the active materials were mixed with PVDF in a N-Methly-2-pyrrolidon (NMP) solution and carbon black (Super P, Alfa Aesar) with a weight ratio of 70:15:15. For the electrodes with PEO as the binder, the active material NFMO, PEO and $NaPF_6$ (PEO: $NaPF_6$ with molar ratio of 16:1) were mixed in acetonitrile with carbon black (Super P, Alfa Aesar) in a 70:15:15 weight ratio with a thinky mixer (model ARV-310).

The slurry was casted by using a doctor blade onto a 12 µm thick aluminium foil (Carl-Roth). Initially, the tapes were dried on a heating plate at a temperature of 120 °C for 1 h and then pressed in an isostatic press. Round shaped cathode electrodes with a diameter of 11 mm were then punched out of the tapes and dried overnight under a high vacuum. The cathodes were tested electrochemically against Na-metal with combining Celgard 2500 and glass fiber separators (Whatman GF/D) and assembled in CR2032-type coin cells or Swagelok cells (Al/Mo/Ni series). 0.9 M $NaPF_6$ (Sigma-Aldrich, 98%) and 0.1 M $NaBF_4$ (Sigma-Aldrich, 98%) dissolved in diethylene glycol-dimethyl ether (Sigma-Aldrich, anhydrous 99.5%) was used as the electrolyte. The electrochemical tests were carried out using a BioLogic MPG-200 potentiostate equipped with a climate chamber.

Cycling protocol

The cycling protocol for the long-term experiments to investigate the behavior of the two different binder PVDF/PEO started with recording open circuit voltage (OCV) for 24 h, followed by a CV experiment which was carried out within a potential window of 1.5–4 V vs. Na/Na^+ with a scanning rate of 0.02 mV/s. Afterwards, galvanostatic charge/discharge cycles measurements were performed at a current density of 0.024 mA/cm² in the potential range of 1.5–4 V vs. Na/Na^+ with a C-rate of 0.05 over 100 cycles.

The cycling protocol for the C-rate test started with 12 h of OCV, followed by galvanostatic charge/discharge tests within the 1.5–4 V potential range vs. Na/Na^+. Five cycles were performed at each rate of 0.05 C, 0.1 C, 0.2 C, 0.1 C, and 0.05 C.

Results and discussion

Slurry preparation

One of the most critical steps in battery cell development is the fabrication of homogeneous cathode and anode sheets free of agglomerates. In addition to the active material, electrode preparation involves a conductive additive (e.g., carbon black), a polymeric binder (e.g., PVDF) to ensure mechanical integrity, and a suitable solvent such as NMP. As illustrated in Fig. 1a, this process comprises four key steps for producing sheets based on the active cathode material NFMO for SIBs. In the first step, the active material and carbon black are ground in a mortar to ensure homogeneous distribution of the conductive additive. In parallel, PVDF is dissolved in NMP at room temperature. The components are merged in a 70:15:15 ratio, with the powder mixture gradually added to the PVDF solution and stirred for up to 4 h to form a homogeneous slurry. The slurry is then cast onto Al foil serving as the current collector.

However, it was observed that even after short periods without stirring, gelation occurs, preventing uniform coating of the aluminum foil (Fig. 1b). PVDF is known to undergo base-induced reactions that can lead to gel formation [29–31]. Figure 1c schematically illustrates a cathode in which defluorinated and crosslinked PVDF surrounds the NFMO/carbon black particles, along with the proposed NaOH-induced β-elimination mechanism responsible for defluorination [21]. In this mechanism, a base-mediated deprotonation by OH^- initially generates a carbanion intermediate, followed by the elimination of NaF and the formation of conjugated polyene chains and forming a gel [21, 30, 32, 33]. Subsequent radical-mediated reactions or coupling between these unsaturated segments may lead to partial crosslinking of PVDF, contributing to gelation of the binder [21, 30, 32, 33]. LTMOs are sensitive to humidity and CO_2. Even if the powder is transferred to a protective atmosphere immediately after synthesis, H_2O and CO_2 can be absorbed at the particle surfaces [34]. This leads to the formation of NaOH and Na_2CO_3, which is also confirmed for NFMO by TGA measurement (Figure 1 Supporting Information) and initializes the defluorination reaction.

PEO serves as a non-fluorinated reference binder for evaluating PVDF defluorination (Fig. 1d). Due to its lack of ionic conductivity, $NaPF_6$ is required for slurry preparation. The polymer is considered inert toward NaOH, maintaining linear chain structures during processing (Fig. 1e). To demonstrate that PEO remains a linear polymer when used as a binder and to confirm the occurrence of crosslinking in PVDF, various sample systems were prepared and analyzed by XRD, which are listed in Table 1.

Quantitative phase analysis

To investigate the defluorination reaction of PVDF in the presence of a base, QPA and Rietveld refinement of measured XRD diffractograms of different samples, listed in Table 1, were conducted (Fig. 2 and Figure S2 Supporting Information).

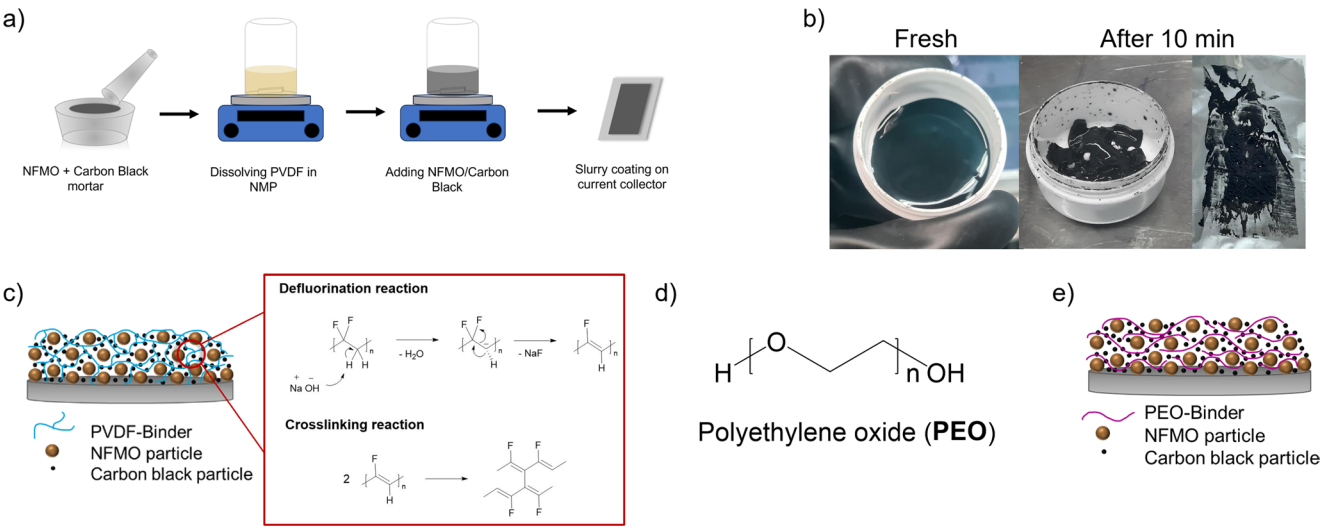

Fig. 1 Schematic illustration of slurry preparation using PVDF as a binder (**a**). Images of fresh and after 10 min slurry with PVDF (**b**). Schematic illustration of composition of a cathode with PVDF as a binder, as well as the possible deflourination reaction of PVDF (**c**). Structural formula of PEO (**d**). Schematic illustration of composition of a cathode with PEO as a binder (**e**)

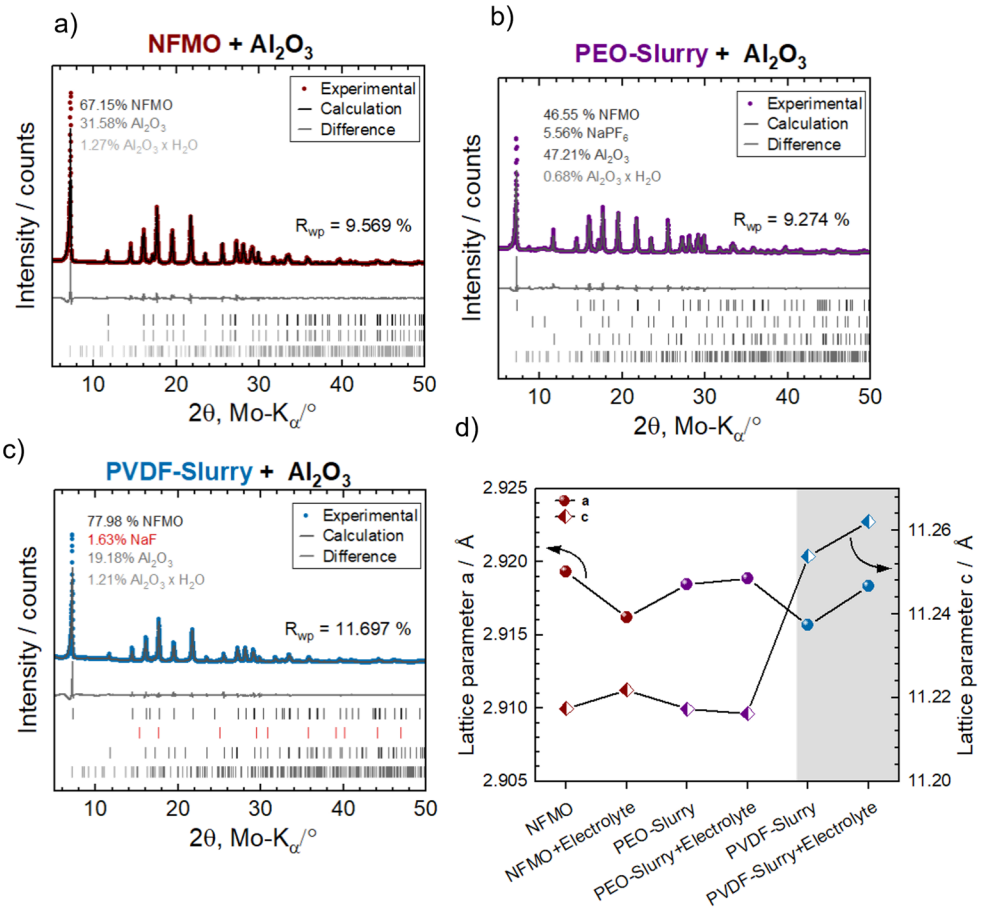

Fig. 2 QPA of NFMO (**a**), PEO-slurry (**b**), PVDF-slurry (**c**) and determined lattice parameter form QPA (**d**)

To accurately determine the changes in lattice parameter, an internal standard Al_2O_3 was mixed to the samples in a ratio of 30:70. Firstly, Al_2O_3 (ICSD code 9770) was used as a starting model to determine lattice parameter, size and strain using the Pawley method [35]. In the QPA and Rietveld refinement analysis the scale factor, thermal Debye Waller factors and occupancies and phase proportions were refined. The internal standard consists of 96.27 wt.-% Al_2O_3 and 3.73 wt.-% $(Al_2O_3)_{11}(H_2O)_{1.73}$ (Figure 2 Supporting Information). All values obtained for the standard were fixed for fitting the data of the other samples. In all samples the main phase NFMO (ICSD code 231006) [36] with a hexagonal $P6_3/mmc$ space group was used as a starting mode. Again, lattice parameter, size and strain were determined using Pawley method and for QPA and Rietveld refinement analysis the scale factor, thermal Debye Waller factors and occupancies and phase proportions were refined, Fig. 2 and Supporting Information Figure 3. The analysis for NFMO+Al_2O_3 (Fig. 2a) reveals 67.15 wt.-% of NFMO, 31.58 wt.-% of Al_2O_3 and 1.27 wt.-% of $(Al_2O_3)_{11}(H_2O)_{1.73}$. The lattice parameter of NFMO could be determined as a_{hex} = 2.91932(6) Å and c_{hex} = 11.2174(4) Å which are consistent with the reported values for this cathode material [12, 36, 37].

The sample NFMO+ Al_2O_3 in electrolyte (Figure S3a, Supporting Information) has the following composition: 46.00 wt.-% NFMO, 7.95 wt.-% $NaPF_6$, 5.99 wt.-% $NaBF_4$, 37.77 wt.-% Al_2O_3 and 2.29 wt.-% $(Al_2O_3)_{11}(H_2O)_{1.73}$. The electrolyte consists of 0.9 M $NaPF_6$ and 0.1 M $NaBF_4$ dissolved in diglyme, which explains the reflexes of the salts. Newly observed reflexes at 5.34°, 8.87°, 9.07° and 10.29° (2θ) could not be assigned to any known crystalline phase. The lattice parameters of NFMO, a_{hex} = 2.91621(13) Å and c_{hex} = 11.2218(8) Å, show only a slight change in comparison to pristine NFMO, with a minimal decrease of 0.003118 Å and an increase of 0.0044 Å, respectively. The sample PEO-slurry+Al_2O_3 (Fig. 2b) exhibits 46.55 wt.-% NFMO, 5.56 wt.-% $NaPF_6$, 47.21 wt.-% Al_2O_3 and 0.68 wt.-% $(Al_2O_3)_{11}(H_2O)_{1.73}$. The determined lattice parameters for NFMO, a_{hex} = 2.91845(8) Å and c_{hex} = 11.2173(5) Å, deviate only slightly from those of the pristine material, with 0.000878 and 0.0001. For the sample PEO-slurry+Al2O3 in electrolyte (Figure S3b, Supporting Information), the following phase fractions result from the analysis: 45.57 wt.-% NFMO, 13.41 wt.-% $NaPF_6$, 3.97 wt.-% $NaBF_4$, 36.15 wt.-% Al_2O_3 and 0.89 wt.-% $(Al_2O_3)_{11}(H_2O)_{1.73}$. $NaPF_6$ is present in a higher proportion compared to the other samples, since $NaPF_6$ is used both in the slurry production of

PEO and in the electrolyte. The fit yields values for the NFMO lattice parameters of 2.91884(11) Å and 11.2162(7) Å, which again show only a very small deviation. Similar to the other sample treated with electrolyte, additional reflections at 5.22, 5.47, 945 and 9.72° (2θ) are observed that cannot be correlated with any known crystalline phase.

The analysis of PVDF-Slurry+Al_2O_3 (Fig. 2c) reveals phase fractions of 77.98 wt.-% of NFMO, and 1.63 wt.-% of a new secondary phase NaF, as well as 19.18 wt.-% Al_2O_3 and 1.21 wt.-% $(Al_2O_3)_{11}(H_2O)_{1.73}$ The lattice parameter a_{hex} with 2.91566(9) Å is 0.0036681 Å lower than the pristine powder sample. Whereas the lattice parameter c_{hex} with 11.2538(7) Å increases significantly by 0.0364 Å. For the sample PVDF+Al_2O_3 treated in electrolyte (Figure S3c, Supporting Information) phase fractions of 31.79 wt.-% NFMO, 8.62 wt.-% $NaPF_6$, 0.34 wt.-% $NaBF_4$, 5.50 wt.-% NaF, 49.20 wt.-% Al_2O_3 and 4.55 wt.-% $(Al_2O_3)_{11}(H_2O)_{1.73}$ are determined. For this sample, again, an unidentified reflex appears around 5.84 ° (2θ). Compared to pristine NFMO, the a_{hex} lattice parameter is reduced by 0.00101 Å to 2.91832(9) Å, whereas c_{hex} increases by 0.04466 Å to 11.26209(7) Å.

Undefined reflections between 5° and 9° (2θ) are observed exclusively in the samples treated with electrolyte. Reflections around 5.3° may originate from decomposition products of diglyme, as reported in the literature [38]. The additional reflexes around 9° are likely associated with the decomposition of the dissolved salts ($NaPF_6$ or $NaBF_4$) in diglyme. In addition, only the samples containing PVDF show NaF in a detectable amount. Since NaF is a known byproduct of the defluorination reaction of PVDF, its presence indicates that such a reaction has occurred. In contrast, no new crystalline phases related to polymer decomposition are observed in the PEO-based samples, suggesting the chemical stability of PEO under these conditions.

The NFMO lattice parameters along the c-axis show a significant increase for the PVDF-based samples (Fig. 2d), whereas no notable changes are observed for the other samples. An expansion of the *c*-parameter may be indicative of Na loss from the structure. Upon Na extraction, the layered framework tends to reorganize to maintain structural stability. A reduced Na content leads to weaker interlayer interactions and increased electrostatic repulsion between the negatively charged layers, which results in an expansion along the *c*-axis. The change in the lattice parameter further supports PVDF defluorination and suggests that PEO remains chemically unchanged.

FT-IR spectroscopy

FT-IR spectroscopy was used to investigate the changes in the binding ratios of the polymers PVDF and PEO in the slurry compositions (Fig. 3 and Supporting Information Figure 4). Characteristic IR bands associated with the α, β, and γ phases of PVDF are observed in both pure PVDF and PVDF-slurry without carbon black, Fig. 3a. The spectra for pure PVDF shows a band at 490.85 cm^{-1}, which is characteristic of the α, β, and γ phases of PVDF. Bands that can be assigned only to α-phase are observed at 612.36, 764.25, 879.97 and 1193.38 cm^{-1}. For β -phase bands at 1069.05, 1276.32 and 1404.58 cm^{-1} are visible and the band at 839 cm^{-1} can be assigned to both α- and β - phase. Bands between 2846.29 and 3029.03 cm^{-1} and at 3395.49 cm^{-1} can be attributed to hydroxyl groups, originating from CO_2/H_2O adsorption on the pellet surface from ambient air [29, 39–43].

For the PVDF slurry, similar vibrations are observed. Bands at 880.45 and 1180.85 cm^{-1} are characteristic of the α-phase only, while those at 1070.91, 1402.65, and a newly formed band at 1683.28 cm^{-1} are attributed to the β-phase. The new band at 1683.28 cm^{-1} can be assigned to the formation of C=C bonds [32]. The band at 838.02 cm^{-1} can be assigned again to both α- and β - phases, whereas the band at 764.25 cm^{-1} vanished.

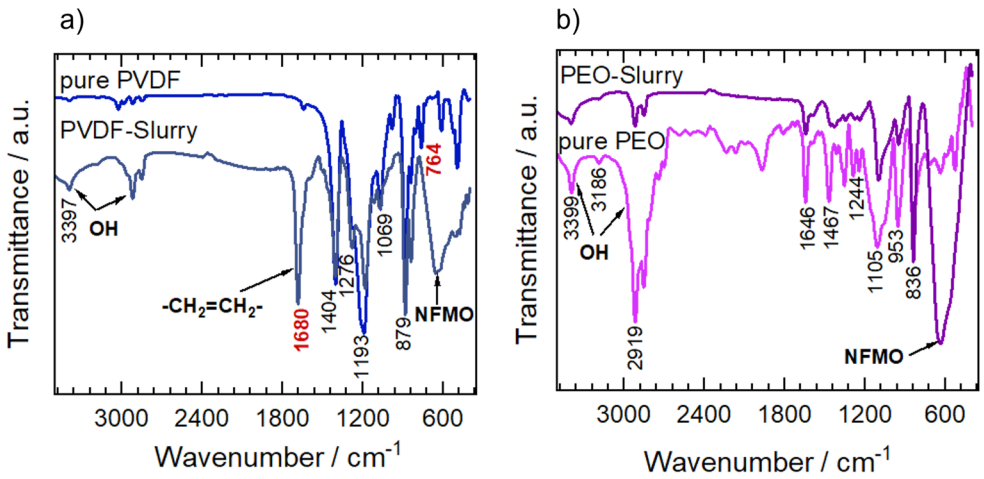

Fig. 3 FT-IR spectra of pure PVDF and PVDF-slurry (**a**) and pure PEO and PEO-slurry (**b**)

Hydroxyl groups are also evident at 2853.04, 2922.47, and 3395.49 cm^{-1}. Furthermore, vibrations corresponding to NFMO are observed in the range of 475–615 cm^{-1} (Figure S4, Supporting Information) [44]. In addition, a well-pronounced band emerging at 1600 cm^{-1} along with the disappearance of the characteristic α-phase band due to C-F bending or rocking vibrations at 764.25 cm^{-1} indicate crosslinking reactions of PVDF induced by NaOH [29, 32, 41–44].This observation is consistent with the XRD results, which show the formation of NaF as a byproduct from the defluorination reaction of PVDF.

In Fig. 3b FT-IR-spectra of pure PEO and PEO-slurry without carbon black is shown. Six characteristic bands for PEO can be assigned in both spectra, the out-of-plane vibration at 951 cm^{-1}, C-O-C stretching vibration at 1107 cm^{-1}, C-O binding at 1249 cm^{-1}, C-O-C binding at 1291 cm^{-1}, CH_2 bending at 1352 cm^{-1} and CH_2 scissoring 1468 cm^{-1} [45, 46]. In the spectra of PEO-slurry the bands for NFMO are visible between 475 and 615 cm^{-1} [44]. All characteristic bands are clearly recognizable in the FT-IR spectra of both the pure PEO and the PEO-slurry. The intensity of the bands in the PEO-slurry is somewhat reduced compared to the pure PEO due to the lower material content in the pellet sample. Nevertheless, all relevant bands are present, which indicates the complete presence of the PEO structure in the slurry. The positional shifts of the bands between the two spectra are minimal. This indicates that the binding conditions for PEO in contact with NFMO remain unchanged. No significant changes in the structure or interactions of PEO with NFMO are observed. These results suggest that no chemical reaction occurs between NFMO and PEO. The polymer remains in its linear structure, and the active material does not react with PEO, which is also confirmed by XRD.

In summary, FT-IR reveals that the binding conditions of the polymer PVDF change during the preparation of the slurry, while the polymer PEO remains unchanged. To further confirm these results and prove the electrochemical stability of PEOs, XPS measurements were performed.

X-ray Photoelectron Spectroscopy

To investigate the electrochemical stability of the different binders, cathodes at various states of charge were analyzed. For PVDF-based electrodes, the C1s and F1s regions were examined for the freshly prepared cathode, after open-circuit voltage (OCV), after charging to 4.2 V vs. Na/Na^+, and after discharging to 1.5 V vs. Na/Na^+ (Fig. 4; Table 2 and Supporting Information Table 1/2).

The C1s region of the freshly prepared cathode using PVDF as a binder exhibits two characteristic peaks with binding energies of 290.9 eV and 286.4 eV, corresponding, respectively, to carbon in $–\underline{C}F_2$ configuration [47–50] and carbon in $\underline{C}H_2–CF_2$ configuration both within the pristine PVDF polymer [47–50]. The latter might also contain a

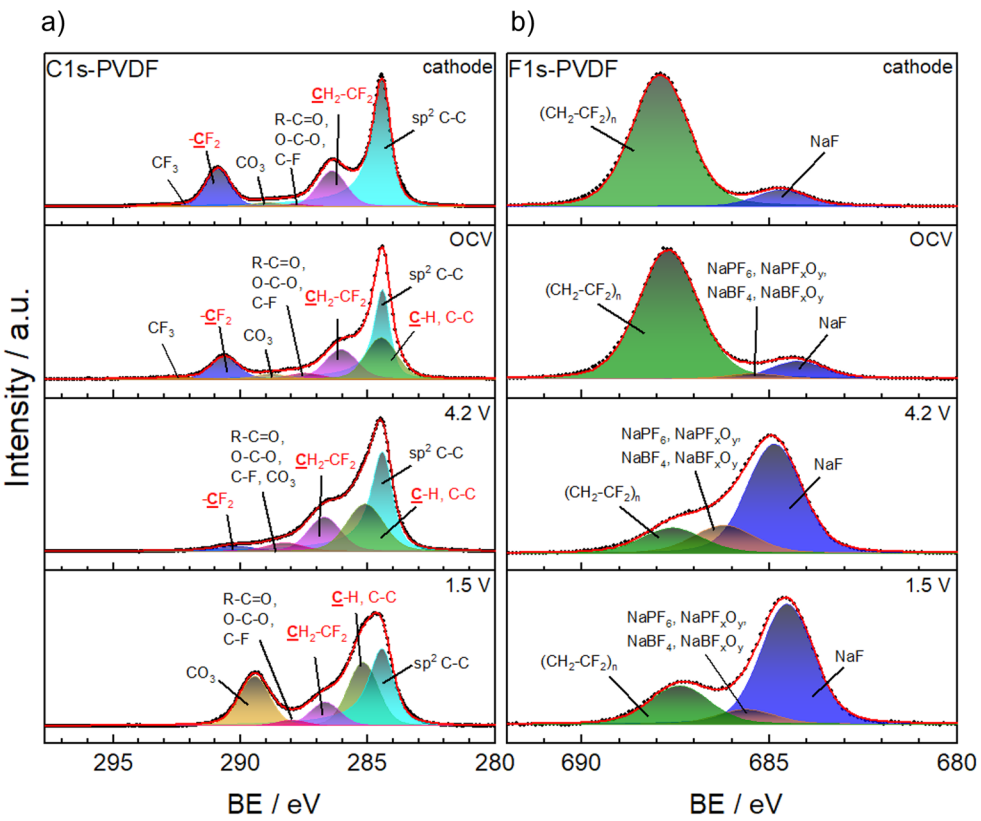

Fig. 4 XPS high-resolution scans recorded for a freshly prepared cathode, a cathode upon cycling at OCV, a cathode upon cycling at 4.2 V, and a cathode upon cycling at 1.5 V, all of which with PVDF as binder: C1s region (**a**) and F1s region (**b**). To account for sample charging during data acquisition, all binding energies were corrected by setting the binding energy of the respective sp^2 C-C peak (stemming from the conductive additive carbon black) to 284.4 eV [43–46]

Table 2 Relative C1s and F1s peak intensities for PVDF-based samples

Sample	C1s		F1s	
	$\underline{\mathbf{C}}H_2$-$CF_2$	CF_2	NaF	CH_2-CF_2
Cathode	18.5%	17.0%	9.9%	90.1%
OCV	18.3%	12.0%	10.6%	86.4%
4.2 V	18.0%	2.9%	64.8%	16.7%
1.5 V	10.3%	0.0%	66.8%	24.0%

small contribution from C-O/ C-O-C species [25–28] due to sample contamination upon air exposure and/ or (e.g. X-ray induced) degradation. Furthermore, a distinct peak with a binding energy of 284.4 eV attributed to carbon in graphitic sp^2 C–C configuration within the carbon black additive is evident [47, 51, 52]. Peak fitting reveals further components with binding energies of 292.6 eV, 287.9 eV and 289 eV. The first two can, respectively, be related to carbon in $\underline{\mathbf{C}}F_3$ configuration [50] as evolved most likely upon X-ray induced polymer degradation [50], and carbon in R-C=O/ O-C-O [25–28] and/ or **C**F configuration [50] due to contamination and PVDF degradation. The third peak can be attributed to CO_3 species [53–55], most likely due to surface carbonation (Table 1/2, Supporting Information).

Similarly, the C1s region of the OCV sample exhibits two peaks with binding energies of 284.4 eV and 290.6 eV which can again be attributed to carbon in graphitic sp^2 C–C and in $\underline{\mathbf{C}}F_2$ configuration, respectively. The latter shows a clear decrease in relative intensity with respect to the freshly prepared cathode, which points to a certain degree of OCV-induced PVDF degradation, particularly PVDF defluorination. Consistently, a decrease in relative $\mathbf{C}H_2$–CF signal intensity occurs, leading to a distinct shoulder with a binding energy of 286.1 eV. Given the composition of the sample, this shoulder also comprises carbon in C-O/ C-O-C configuration within pristine diglyme. Besides, a considerable peak with a binding energy of 284.5 eV suggests the formation of aliphatic C-H/ C-C species, further corroborating evidence of degradation effects. Upon cycling to 4.2 V and 1.5 V, the respective C1s regions are characterized by both a further decrease of the $\mathbf{C}H_2$–CF_2 and $\underline{\mathbf{C}}F_2$ portions as well as an increase of the C-H/ C-C portions, suggesting further modifications in the PVDF chemical environment during cycling. For the sample cycled to 1.5 V, any $\underline{\mathbf{C}}F_2$ signal, even at low intensity, could be masked by the dominant CO_3 peak. A comparison of the relative peak intensities with respect to the overall C1s signal across the different samples (Table 2) shows that the particular $\underline{\mathbf{C}}H_2$–$CF_2$ contribution decreases gradually from an initial 18.5% for the freshly prepared cathode to 18.3% and 18.0% for the OCV and 4.2 V sample, respectively. A minimum of 10.3% is obtained for the sample cycled at 1.5 V. It should be emphasized that these values, except in the case of freshly prepared cathodes, also include a certain proportion of carbon in C-O/C-O-C configurations within pure diglyme (electrolyte). Consistently, the $\underline{\mathbf{C}}F_2$ signal drops from an initial 17% to 12%, 2.9% and 0% for the OCV, 4.2 V and 1.5 V sample, respectively.

Complementary, the F1s region of the freshly prepared cathode shows a strong peak at 687.9 eV, corresponding predominantly to the $(CH_2–CF_2)_n$ units of the pristine PVDF [13, 18, 48–50] (Fig. 4b and Supporting Information Figure 1–3). A second, considerably smaller peak at 684.7 eV, can be attributed to NaF [47, 52]. Both the $(CH_2–CF_2)_n$ and NaF features are likewise observed for all cycled samples. Consistently with the findings obtained from the C1s regions, the NaF peak intensities increase particularly for the electrodes cycled to 1.5 V and 4.2 V. Whereas the respective $(CH_2–CF_2)_n$ peak intensities decrease. Besides, the F1s regions of all three cycled samples exhibit another peak with binding energies between 686.2 eV and 685.4 eV, which can be assigned to pristine electrolyte salts ($NaPF_6$ and $NaBF_4$) and a multitude of its decomposition products ($NaPF_xO_y$/ $NaBF_xO_y$) [47, 52, 56].

The gradual NaF formation upon cycling can again be illustrated by its relative peak intensity (Table 2) with respect to the overall F1s signal for each sample. While for the freshly prepared cathode only a NaF contribution of 9.9% is observed, a clear increase to 10.6% is already noted for the OCV sample. It is evident that any NaF in the pristine cathode solely forms via PVDF defluorination during the slurry process, since no electrolyte was admixed to this sample. The relative NaF peak intensity further increases dramatically for the 4.2 V sample (64.8%), reaching a maximum of 66.8% for the 1.5 V sample. Concurrently, the respective PVDF-related CH_2–CF_2 contributions also decrease substantially (cathode: 90.1%, OCV: 86.4%, 4.2 V: 16.7%, 1.5 V: 24.0%). Besides, the relative peak intensities of the electrolyte and electrolyte-decomposition products (Table S2, Supporting Information) also show a clear trend. Being absent in the pristine cathode, its contribution increases to 3.1% for the OCV sample, reaches a maximum of 18.5% for the 4.2 V sample, and eventually drops to 9.2% for the 1.5 V sample.

Based on the F1s data evaluation of the cathode, it is evident that PVDF defluorination leads to NaF formation, with a significant proportion percentage of 9.9% of the decomposition product. Due to the absence of electrolytes, NaF formation is solely caused by changes in the PVDF during the slurry process. Further gradual PVDF degradation and NaF formation during the cycling process are evidenced by consistent trends of the particular relative C1s and F1s peak intensities.

Comparable samples were examined for PEO-based electrodes: a freshly prepared cathode, after OCV and after charging to 4.0 V vs. Na/Na^+ (Fig. 5; Tables 3 and Supporting Information 1–4).

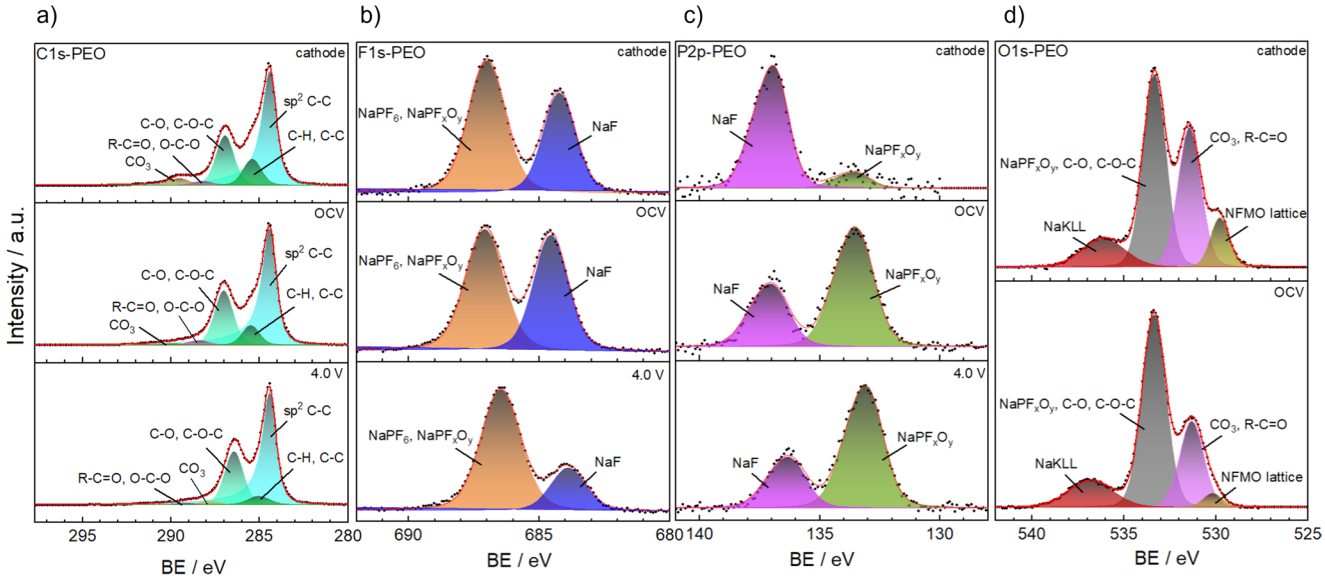

Fig. 5 XPS high-resolution scans recorded for a freshly prepared cathode, a cathode upon cycling at OCV, and a cathode upon cycling at 4.0 V, all of which with PEO as binder: C1s region (**a**), F1s region (**b**), P2ps region (**c**), and O1s region (**d**). To account for sample charging during data acquisition, all binding energies were corrected by setting the binding energy of the respective sp^2 C-C peak (stemming from the conductive additive carbon black) to 284.4 eV [43–46]

Table 3 Relative C1s, F1s and P2p intensities for PEO-based sample

Sample	C1s	F1s	P2p	
	C-O/C-O-C	NaF	$NaPF_6$	$NaPF_xO_y$
Cathode	23.2%	40.0%	88.3%	11.7%
OCV	26.5%	46.0%	34.5%	65.5%
4.0 V	28.2%	24.0%	29.5%	70.5%

The C1s region of the freshly prepared PEO cathode is characterized by two dominant peaks with binding energies of 284.4 eV and 287 eV, which can be attributed to carbon in graphitic sp^2 C–C configuration [47, 51, 52] within the carbon black additive and carbon in C-O/C-O-C configuration [25–28], respectively (Fig. 5a). The latter can also be observed for pure PEO powder reference and thus primarily corresponds to the carbon atoms within the pristine PEO polymer (Figure 5 in Supporting Information). Besides, peak fitting reveals another three peaks with binding energies of 285.4 eV, 288.2 eV and 289.6 eV. The former two are most likely due to C-H/ C-C [25–28] and R-C = O, O-C-O [25–28] contaminations, respectively. The former, can be related to CO_3 species [53–55], evolving for reasons outlined above (Fig. 5a and Supporting Information Tables 1–4). Upon cycling, no significant changes in relative peak contributions occur, which might be indicative of any trend as observed for the PVDF counterpart. A slight increase in the particular relative C-O/ C-O-C contributions upon cycling (OCV: 26.5%, 4.0 V: 28.9%) in comparison to the freshly prepared cathode (23.2%) might be explained by the admixture of diglyme to the former two, Table 3. It can thus be concluded from the C1s region that the PEO polymer chains did not undergo significant degradation or decomposition during the slurry process and upon cycling.

Insight in possible electrolyte decomposition, is provided by a complementary inspection of the respective F1 regions, Fig. 5b. Generally, two well-separated peaks can be observed for each sample. Regarding the freshly prepared cathode, a peak with a binding energy of 687 eV corresponds to $NaPF_6$ and possibly a multitude and $NaPF_xO_y$ species [47, 52, 56]. A second peak with a binding energy of 684.2 eV, in turn, is attributed to NaF [47, 52], which is a decomposition product. Thus, likely, partial $NaPF_6$ decomposition occurs in the solvent acetonitrile used during slurry production. In fact, the relative NaF peak intensity amounts to 40% for the freshly prepared cathode, whereas it is 46.0% and 24.0% for the OCV and 4.0 V sample, respectively (Table 3). As for the latter two, NaF formation most likely occurs via both $NaPF_6$ and $NaBF_4$ decomposition.

In accordance with the F1s signal, the P2p signal provides clear evidence of $NaPF_6$ electrolyte decomposition for the cathode sample as well as both cycled samples (Fig. 5c). It also provides further insight into the particular $NaPF_6$/ $NaPF_xO_y$ ratio, as two, relatively broad peaks, each of which denotes a P2p spin-orbit doublet for either species, can clearly be observed for all samples. For the freshly prepared cathode, the relative contribution of pristine $NaPF_6$ to the overall P2p signal is 88.3%, which corresponds to a dominant peak with a $P2p_{3/2}$ binding energy of 136.8 eV. This figure drops to 34.5% and 29.5% for the

OCV and 4.0 V sample, respectively (Table 3). Accordingly, the relative contributions of $NaPF_xO_y$ decomposition products increase. While it amounts to a mere 11.7% for the freshly prepared cathode, corresponding to rather small peak with a $P2p_{3/2}$ binding energy of 133.4 eV, it increases significantly to 65.5% and 70.5% for the OCV and 4.0 sample, respectively. In fact, this trend does not only indicate acetonitrile-triggered electrolyte decomposition, but also further gradual electrolyte decomposition upon cycling.

The O1s regions of the cathode and the OCV sample exhibit peaks corresponding to the NFMO lattice, CO_3/R-C=O, $NaPF_xO_y$/C-O/C-O-C, and as well as a Na KLL Auger peak, which is typically observed for Na-containing samples (Fig. 5d). Apart from the decreasing intensity of the NFMO lattice oxide peak for the OCV sample, no significant changes occur.

In summary, the XPS results align with the FT-IR results, indicating that PVDF undergoes a defluorination reaction in the presence of a base. Furthermore, the findings indicate that PVDF undergoes additional electrochemical changes or degradation processes during cycling. In contrast, PEO remains chemically and electrochemically unchanged with only the admixed electrolytes being considerably affected.

Electrochemistry

To investigate the electrochemical influence of the defluorination reaction of PVDF and PEO as a binder for cathode materials, cyclic voltammetry (CV), C-rate tests and galvanostatic charge/discharge experiments at a 0.05 C-rate between 1.5 and 4.0 V vs. Na/Na^+ were carried out (Fig. 6). Since PEO is unstable at high potentials, the window is limited to 4.0 V vs. Na/Na^+ [57].

Figures 6a/b present CV measurements of NFMO electrodes employing PVDF and PEO binders. Both samples exhibit a distinct oxidation peak at 2.23 V vs. Na/Na^+ and a corresponding reduction peak at 2.03 V vs. Na/Na^+, which can be attributed to the reversible redox reaction of the $Mn^{3+/4+}$ couple. In both cases, the redox process is reversible. However, in the case of the NFMO-PVDF electrode, the peak current decreases with increasing cycle number, and the oxidation peaks broaden progressively, indicating ongoing side reactions and incomplete electrochemical stabilization. In contrast, the NFMO-PEO electrode displays highly reversible redox behavior with minimal peak broadening and less pronounced current decay, suggesting fewer side reactions and improved electrochemical stability.

For the C-rate test five cycles were recorded for NFMO-PVDF/PEO for each C-rate (0.05C, 0.1C, 0.2C, 0.1C,

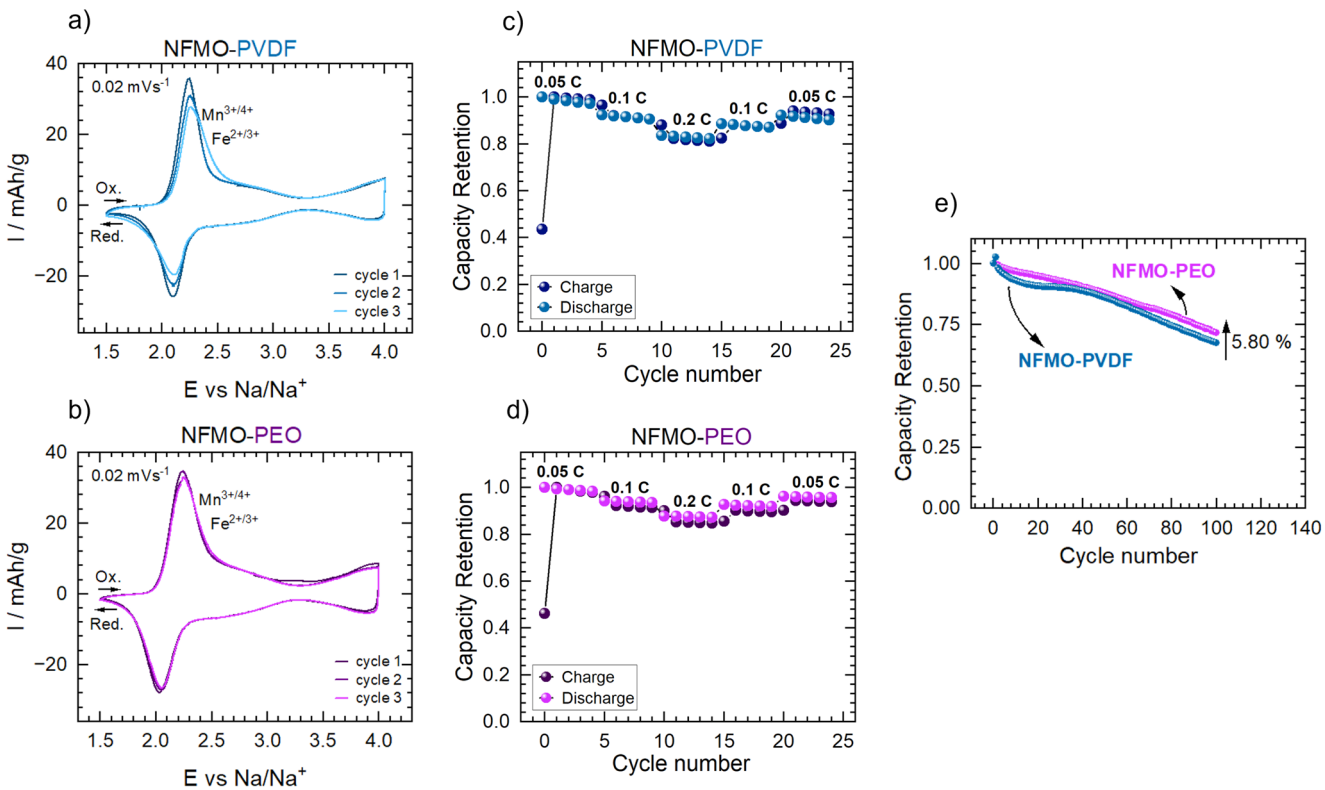

Fig. 6 Cyclovoltammogram of NFMO-PVDF (**a**) and NFMO-PEO (**b**) between 1.5–4.0 V vs. Na/Na^+. C-rate test in half cells gaianst Na-metal between 1.5–4.0 V of NFMO-PVDF (**c**) and NFMO-PEO (**d**).). Discharge capacity retention of NFMO-PVDF and NFMO-PEO of GCPL measurements between 1.5–4.0 V vs. Na/Na^+ (**e**)

0.05C) between 1.5 and 4 V vs. Na/Na^+, Fig. 6c/d. Upon completion of five cycles at a C-rate of 0.2C for NFMO-PVDF, the discharge capacity retention was found to be 82.2%. After the final five cycles at a reduced C-rate of 0.05C, the discharge capacity retention increased again to 90.31%, indicating favorable cell recovery. In comparison, NFMO-PEO exhibits a discharge capacity retention of 87.26% after five cycles at a C-rate of 0.2C, approximately 5% better than the PVDF sample. After the final five cycles at 0.05C, a discharge capacity retention of 95.67% remains. This represents an improvement of 5.36% compared to the PVDF-based sample. The NFMO-PEO electrode exhibits superior capacity recovery compared to its PVDF-based counterpart. This supports the hypothesis that the defluorination reaction and the resulting cross-linking processes influence the electrochemical reaction, particularly regarding capacity retention.

The galvanostatic charge/discharge experiments, Fig. 6e, show after 100 charge/discharge cycles, continuous degradation for both NFMO-PVDF and NFMO-PEO. The temporary capacity increase observed for NFMO-PVDF could be attributed to a gradual activation process during the first few cycles. This is likely due to the relatively poor wettability by the electrolyte and the lower ionic conductivity of PVDF, which delay the complete penetration of the electrolyte and the full utilization of the active material [20, 58, 59]. NFMO-PEO initially exhibits only minor degradation after 10 cycles (capacity retention of approximately 0.98), followed by a more pronounced decline up to cycle 20. Between cycles 20 and 100, there is a steady decline in capacity retention. This indicates that PEO possesses a lower degradation compared to PVDF. After 100 cycles NFMO-PVDF retains only 68% of its initial capacity, whereas NFMO-PEO remains 72%. This demonstrates that the PEO-based sample exhibits 5.8% better performance compared to its PVDF-based counterpart. Conducting cycle tests at a low current density (C/20) minimizes kinetic polarization and transport limitations, thereby highlighting the chemical and interfacial stability of the binders, which is reflected in improved cycle stability. This improvement in capacity retention is consistent with the FT-IR and XPS results, which confirm the chemical and electrochemical degradation of PVDF-based electrodes, while the PEO binder remains stable.

The strong capacity degradation in both samples, NFMO-PVDF/PEO, is typical for the cathode material P2-NFMO due to the irreversible phase transition during sodation/desodation [36, 37]. PEO as a binder using conductive salt, in this case $NaPF_6$, is ionically conductive, which could promote the transport of Na^+. In addition to the defluorination of PVDF and the resulting polymer crosslinking, the intrinsic non-conductivity of PVDF could hinder Na^+ ion mobility. These factors contribute to the improved capacity retention observed when PEO is employed as a binder. Studies published in the literature have also demonstrated improved electrochemical performance through the use of PEO as a binder, which is attributable to improved adhesion of the electrode components and electrode integrity, resulting in improved cycle stability and reduced electrode resistance [20].

Conclusion

This study investigated the base-induced defluorination of PVDF binders in cathode materials, using NFMO as the active material. PEO was employed as a non-fluorinated binder system, as it is not expected to undergo chemical reactions under alkaline conditions, enabling a direct comparison with the fluorinated binder PVDF. FT-IR spectroscopy revealed additional bands in PVDF-based slurry, indicating changes in the polymer structure, while PEO-slurry remained unaffected. XPS analysis confirmed the chemical and electrochemical stability of PEO, whereas NaF formation in PVDF-based electrodes provided clear evidence of binder defluorination. Moreover, PVDF was found to undergo progressive degradation during cycling. Electrolyte decomposition was observed in both systems during charge/discharge processes. Furthermore, long-term electrochemical measurements showed that PEO-based electrodes exhibited a moderate 5.8% improvement in performance after 100 cycles compared to PVDF, suggesting that progressive degradation of PVDF is likely to impair long-term performance. However, due to its limited suitability for high-voltage applications, PEO cannot be considered a universal alternative but rather serves as a non-fluorinated model system to highlight the influence of defluorination in PVDF-based binders. Therefore, the development of chemically stable binder systems remains essential for SIB cathodes, particularly for air-sensitive layered LTMOs.

Supplementary Information The online version contains supplementary material available at https://doi.org/10.1007/s10008-026-06668-z.

Acknowledgements This work was financially supported by the project "High Performance Solid-State Batteries" (HIPSTER) from "Ministerium für Kultur und Wissenschaft des Landes Nordrhein-Westfalen" from Bundesministerium für Bildung und Forschung.

Data availability Data related to this study are available in repository at the following link: https://doi.org/10.26165/JUELICH-DATA/XIHKGR.

Declarations

Competing interests The authors declare no conflict of interest.

References

1. Gupta Y, Siwatch P, Karwasra R et al (2024) Recent progress of layered structured P2- and O3- type transition metal oxides as cathode material for sodium-ion batteries. Renew Sustain Energy Rev 192:114167. https://doi.org/10.1016/j.rser.2023.114167
2. Tang K, Wang Y, Zhang X et al (2019) High-performance P2-Type Fe/Mn-based oxide cathode materials for sodium-ion batteries. Electrochim Acta 312:45–53. https://doi.org/10.1016/j.electacta.2019.04.183
3. Li P, Yuan T, Qiu J et al (2025) A comprehensive review of layered transition metal oxide cathodes for sodium-ion batteries: The latest advancements and future perspectives. Mater Sci Engineering: R: Rep 163:100902. https://doi.org/10.1016/j.mser.2024.100902
4. Peng B, Zhou Z, Shi J et al (2024) Earth-Abundant Fe-Mn-Based Compound Cathodes for Sodium-Ion Batteries: Challenges and Progress. Adv Funct Mater 34. https://doi.org/10.1002/adfm.202311816
5. Cui J, Li Z, Di Zhang et al (2024) Recent advances of in-situ spectroscopic analysis for cathode materials of sodium-ion batteries. J Energy Storage 97:112734. https://doi.org/10.1016/j.est.2024.112734
6. Baumann M, Häringer M, Schmidt M et al (2022) Prospective Sustainability Screening of Sodium-Ion Battery Cathode Materials. Adv Energy Mater 12. https://doi.org/10.1002/aenm.202202636
7. Delmas C, Fouassier C, Hagenmuller P (1980) Structural Classification and Properties of the Layered Oxides. Physica 81–85. https://doi.org/10.1016/0378-4363(80)90214-4
8. Wang P-F, You Y, Yin Y-X et al (2018) Layered Oxide Cathodes for Sodium-Ion Batteries: Phase Transition, Air Stability, and Performance. Adv Energy Mater 8. https://doi.org/10.1002/aenm.201701912
9. Wang X, Roy S, Shi Q et al (2021) Progress in and application prospects of advanced and cost-effective iron (Fe)-based cathode materials for sodium-ion batteries. J Mater Chem A 9:1938–1969. https://doi.org/10.1039/D0TA10610K
10. Zuo W, Xiao Z, Zarrabeitia M et al (2022) Guidelines for Air-Stable Lithium/Sodium Layered Oxide Cathodes. ACS Mater Lett 4:1074–1086. https://doi.org/10.1021/acsmaterialslett.1c00827
11. Xu C, Cai H, Chen Q et al (2022) Origin of Air-Stability for Transition Metal Oxide Cathodes in Sodium-Ion Batteries. ACS Appl Mater Interfaces 14:5338–5345. https://doi.org/10.1021/acsami.1c21103
12. Zhao J, Xu J, Lee DH et al (2014) Electrochemical and thermal properties of P2-type Na2/3Fe1/3Mn2/3O2 for Na-ion batteries. J Power Sources 264:235–239. https://doi.org/10.1016/j.jpowsour.2014.04.048
13. Chou S-L, Pan Y, Wang J-Z et al (2014) Small things make a big difference: binder effects on the performance of Li and Na batteries. Phys Chem Chem Phys 16:20347–20359. https://doi.org/10.1039/c4cp02475c
14. Li R-R, Yang Z, He X-X et al (2021) Binders for sodium-ion batteries: progress, challenges and strategies. Chem Commun (Camb) 57:12406–12416. https://doi.org/10.1039/d1cc04563f
15. Lv M, Zhao R, Hu Z et al (2024) Binder design strategies for cathode materials in advanced secondary batteries. Energy Environ Sci 17:4871–4906. https://doi.org/10.1039/D4EE00791C
16. Srivastava M, AK MR, Zaghib K (2024) Binders for Li-Ion Battery Technologies and Beyond: A Comprehensive Review. Batteries 10:268. https://doi.org/10.3390/batteries10080268
17. Qin T, Yang H, Li Q et al (2024) Design of functional binders for high-specific-energy lithium-ion batteries: from molecular structure to electrode properties. Ind Chem Mater 2:191–225. https://doi.org/10.1039/D3IM00089C
18. Kang G, Cao Y (2014) Application and modification of poly(vinylidene fluoride) (PVDF) membranes – A review. J Membr Sci 463:145–165. https://doi.org/10.1016/j.memsci.2014.03.055
19. Zhang Z, Zeng T, Lai Y et al (2014) A comparative study of different binders and their effects on electrochemical properties of LiMn 2 O 4 cathode in lithium ion batteries. J Power Sources 247:1–8. https://doi.org/10.1016/j.jpowsour.2013.08.051
20. Mo J, Zhang D, Sun M et al (2021) Polyethylene Oxide as a Multifunctional Binder for High-Performance Ternary Layered Cathodes. Polym (Basel) 13. https://doi.org/10.3390/polym13223992
21. Hsieh C-T, Wu W, Eeso K et al (2025) Unveiling the Reactivity of Fluoropolymers with Sodium Metal: Mechanistic Insights and Battery Implications. JACS Au 5:3513–3520. https://doi.org/10.1021/jacsau.5c00552
22. Vogt LO, El Kazzi M, Jämstorp Berg E et al (2015) Understanding the Interaction of the Carbonates and Binder in Na-Ion Batteries: A Combined Bulk and Surface Study. Chem Mater 27:1210–1216. https://doi.org/10.1021/cm5039649
23. Sudhakaran S, Bijoy TK (2023) A Comprehensive Review of Current and Emerging Binder Technologies for Energy Storage Applications. ACS Appl Energy Mater 6:11773–11794. https://doi.org/10.1021/acsaem.3c02218
24. Domgans A, Tran NTT, Speer S et al (2026) Selective Halide Incorporation in P2-Na 0.66 Fe 1/3 Mn 2/3 O 2 Cathodes: Revealing a Compositional Regime for Enhanced Cycling. Small Struct 7. https://doi.org/10.1002/sstr.202500808
25. Biesinger MC (2022) Accessing the robustness of adventitious carbon for charge referencing (correction) purposes in XPS analysis: Insights from a multi-user facility data review. Appl Surf Sci 597:153681. https://doi.org/10.1016/j.apsusc.2022.153681
26. Biesinger MC, Lau LWM, Gerson AR et al (2012) The role of the Auger parameter in XPS studies of nickel metal, halides and oxides. Phys Chem Chem Phys 14:2434–2442. https://doi.org/10.1039/c2cp22419d
27. Gengenbach TR, Major GH, Linford MR Practical guides for x-ray photoelectron spectroscopy (XPS): Interpreting the carbon 1s spectrum. Journal of Vacuum ScienceTechnology, Vacuum A et al (2021) Surfaces, and Films 39. https://doi.org/10.1116/6.0000682
28. Grey LH, Nie H-Y, Biesinger MC (2024) Defining the nature of adventitious carbon and improving its merit as a charge correction reference for XPS. Appl Surf Sci 653:159319. https://doi.org/10.1016/j.apsusc.2024.159319
29. Wootthikanokkhan J, Changsuwan P (2008) Dehydrofluorination of PVDF and Proton Conductivity of the Modified PVDF/Sulfonated SEBS Blend Membranes. J Met Mater Minerals 18:57–62
30. Roberts S, Chen L, Kishore B et al (2022) Mechanism of gelation in high nickel content cathode slurries for sodium-ion batteries. J Colloid Interface Sci 627:427–437. https://doi.org/10.1016/j.jcis.2022.07.033
31. Nguyen T (1985) Degradation of Poly[vinyl Fluoride] and Poly[vinylidene Fluoride]. J Macromolecular Sci Part C 25:227–275. https://doi.org/10.1080/15583728509412823
32. Sharma J, Totee C, Kulshrestha V et al (2023) Spectroscopic evidence and mechanistic insights on dehydrofluorination of PVDF in alkaline medium. Eur Polymer J 201:112580. https://doi.org/10.1016/j.eurpolymj.2023.112580
33. Ahmed MM, Hrůza J, Stuchlík M et al (2021) Revisiting the polyvinylidene fluoride heterogeneous alkaline reaction mechanism in propan-2-ol: An additional hydrogenation step. Eur Polymer J 156:110605. https://doi.org/10.1016/j.eurpolymj.2021.110605
34. Yao H-R, Zheng L, Xin S et al (2022) Air-stability of sodium-based layered-oxide cathode materials. Sci China Chem 65:1076–1087. https://doi.org/10.1007/s11426-022-1257-8

35. Pawley GS (1980) the Edinburgh powder profile refinement program. J Appl Cryst 630633. https://doi.org/10.1107/S0021889880012964
36. Mortemard de Boisse B, Carlier D, Guignard M et al (2018) Influence of Mn/Fe Ratio on Electrochemical and Structural Properties of P2-Na x Mn 1– y Fe y O 2 Phases as Positive Electrode Material for Na-Ion Batteries. Chem Mater 30:7672–7681. https://doi.org/10.1021/acs.chemmater.8b02953
37. Ding C, Nohira T, Hagiwara R (2017) Charge-discharge performance of Na 2/3 Fe 1/3 Mn 2/3 O 2 positive electrode in an ionic liquid electrolyte at 90°C for sodium secondary batteries. Electrochim Acta 231:412–416. https://doi.org/10.1016/j.electacta.2017.02.069
38. Wang Y, Wang X, Zhao B et al (2024) Molecular-level identification of organic species of ether-based solid-electrolyte interphase in sodium-ion batteries. Nano Energy 120:109163. https://doi.org/10.1016/j.nanoen.2023.109163
39. Liu L, Fu W, Wang L et al (2021) Dopamine-coated nano-SiO 2 -modified PVDF piezoelectric composite film. New J Chem 45:11544–11551. https://doi.org/10.1039/D1NJ01153G
40. Botero ER, Nobrega JAE, Trombini DC et al (2020) Influence of NiFe2O4 on β phase formation in PVDF composites. https://doi.org/10.15406/mseij.2020.04.00131. MSEIJ 4
41. Cai X, Lei T, Sun D et al (2017) A critical analysis of the α, β and γ phases in poly(vinylidene fluoride) using FTIR. RSC Adv 7:15382–15389. https://doi.org/10.1039/C7RA01267E
42. Li J, Meng Q, Li W et al (2011) Influence of crystalline properties on the dielectric and energy storage properties of poly(vinylidene fluoride). J Appl Polym Sci 122:1659–1668. https://doi.org/10.1002/app.34020
43. Wang E, Wang H, Hu Y et al (2017) Corrosion-resistant engineering superhydrophobic and superoleophilic bulk materials with oil–water separation property. J Mater Sci 52:7130–7139. https://doi.org/10.1007/s10853-017-0948-2
44. Rahmawati F, Kusumaningtyas AA, Saraswati TE et al (2021) Mn-doped NaFeO 2 from a low purity-Fe precursor and its performance as cathode for Sodium-Ion Battery. Inorg Nano-Metal Chem 51:383–390. https://doi.org/10.1080/24701556.2020.1790003
45. Abdelrazek EM, Abdelghany AM, Badr SI, Morsi MA (2016) Evaluation of optical parameters and structural variations of UV irradiated (PEO/PVP)/Au polymer nanocomposites. Res J Pharm Biol Chem Sci 7:1877–1890
46. Roy A, Dutta B, Bhattacharya S (2017) Ion dynamics in NaBF4 salt-complexed PVC–PEO blend polymer electrolytes: correlation between average ion hopping length and network structure. Ionics 23:3389–3399. https://doi.org/10.1007/s11581-017-2154-2
47. Zarrabeitia M, Rojo T, Passerini S et al (2022) Influence of the Current Density on the Interfacial Reactivity of Layered Oxide Cathodes for Sodium-Ion Batteries. https://doi.org/10.1002/ente.202200071. Energy Tech 10
48. Militello MC, Gaarenstroom SW (1999) Graphite-Filled Poly(vinylidene fluoride) (PVdF) by XPS. Surf Sci Spectra 6:141–145. https://doi.org/10.1116/1.1247908
49. Sarkar S, Garain S, Mandal D et al (2014) Electro-active phase formation in PVDF–BiVO 4 flexible nanocomposite films for high energy density storage application. RSC Adv 4:48220–48227. https://doi.org/10.1039/C4RA08427F
50. Nansé G, Papirer E, Fioux P et al (1997) Fluorination of carbon blacks: An X-ray photoelectron spectroscopy study: I. A literature review of XPS studies of fluorinated carbons. XPS investigation of some reference compounds. Carbon 175–194. https://doi.org/10.1016/S0008-6223(96)00095-4
51. Kaciulis S (2012) Spectroscopy of carbon: from diamond to nitride films. Surf Interface Anal 44:1155–1161. https://doi.org/10.1002/sia.4892
52. Ghosh S, Rana A, Mohini A et al (2025) Decoding Anode Stability: From Nucleation Kinetics to Pattern-Guided Flux Control for Long-Cycling Anode-Less Sodium Metal Batteries. Adv Energy Mater. https://doi.org/10.1002/aenm.202503588
53. Fondard J, Irisarri E, Courrèges C et al (2020) SEI Composition on Hard Carbon in Na-Ion Batteries After Long Cycling: Influence of Salts (NaPF 6, NaTFSI) and Additives (FEC, DMCF). J Electrochem Soc 167:70526. https://doi.org/10.1149/1945-7111/ab75fd
54. Li J, Hao J, Yuan Q et al (2024) The effect of salt anion in ether-based electrolyte for electrochemical performance of sodium-ion batteries: A case study of hard carbon. Carbon Energy 6. https://doi.org/10.1002/cey2.518
55. Muñoz-Márquez MA, Zarrabeitia M, Castillo-Martínez E et al (2015) Composition and evolution of the solid-electrolyte interphase in Na2Ti3O7 electrodes for Na-ion batteries: XPS and Auger parameter analysis. ACS Appl Mater Interfaces 7:7801–7808. https://doi.org/10.1021/acsami.5b01375
56. Ma M, Cai H, Xu C et al (2021) Engineering Solid Electrolyte Interface at Nano-Scale for High-Performance Hard Carbon in Sodium-Ion Batteries. Adv Funct Mater 31. https://doi.org/10.1002/adfm.202100278
57. Wu X, Whitacre JF (2023) Reevaluating the stability of the PEO-based solid-state electrolytes for high voltage solid-state batteries. J Energy Storage 63:107052. https://doi.org/10.1016/j.est.2023.107052
58. Zhang L, Wu X, Qian W et al (2023) Exploring More Functions in Binders for Lithium Batteries. Electrochem Energy Rev 6. https://doi.org/10.1007/s41918-023-00198-2
59. Zheng M, Wang Y, Reeve J et al (2018) A Polymer-Alloy Binder for Structures-Properties Control of Battery Electrodes. Energy Storage Mater 14:149–158. https://doi.org/10.1016/j.ensm.2018.03.006

Publisher's note Springer Nature remains neutral with regard to jurisdictional claims in published maps and institutional affiliations.

Springer Nature or its licensor (e.g. a society or other partner) holds exclusive rights to this article under a publishing agreement with the author(s) or other rightsholder(s); author self-archiving of the accepted manuscript version of this article is solely governed by the terms of such publishing agreement and applicable law.